Optics Letters

# Reconfigurable and tunable terahertz wrench-shape metamaterial performing programmable characteristic

Zefeng Xu, Zhicheng Lin, Shaojun Cheng, and Yu-Sheng Lin*

*State Key Laboratory of Optoelectronic Materials and Technologies, School of Electronics and Information Technology, Sun Yat-Sen University, Guangzhou 510275, China*
**Corresponding author: linyoush@mail.sysu.edu.cn*

*Received 25 June 2019; accepted 10 July 2019; posted 11 July 2019 (Doc. ID 370925); published 6 August 2019*

**A design of a tunable terahertz (THz) programmable device by using wrench-shape metamaterial (WSM) is presented, which is composed of a Au layer fabricated on a Si substrate. The size of the WSM unit cell is 30 μm × 30 μm, and the distance between each WSM is 20 μm. The electromagnetic response of the THz programmable device exhibits the switch function for single-band resonance and dual-band resonance at the transverse electric mode and transverse magnetic mode. The resonance spans from 3.00 to 8.00 THz and is insensitive to the angle of the incident THz wave. While changing the incident angle of the THz wave, the bandwidth of the resonance becomes broader and the transmission spectrum decreases gradually. By configuring the unit cell from single-atom to quad-atom, WSM exhibits optical-logic behaviors with programmable characteristics and anti-interference. Such results are very suitable for use for an ultra-narrowband filter, single-/dual-band switch, polarization switch, and programmable device. It could potentially provide all-optical logical devices with multichannel data processing at higher bit rates.** 

https://doi.org/10.1364/OL.44.003944

Terahertz (THz) generally refers to the electromagnetic (EM) wave in the frequency range of 0.1–10 THz, which is located between the infrared (IR) and microwave spectra. It is the transition stage from macroscopic electronics to microscopic photonics [1,2]. In early times, the THz spectrum had different names in various fields, which is called far IR in the optical field, submillimeter wave or ultra-microwave in the electronic field, and so on [3]. The THz EM wave has many unique properties. These unique optical properties offer widespread applications in the THz EM wave, which has high permeability showing good penetration of many dielectric materials and non-polar substances. It can be applied in perspective imaging for opaque objects. This characteristic is effectively complementary to X-ray imaging and ultrasonic imaging technologies to be used in security or quality (Q) inspection with nondestructive testing [4–6]. In addition, the THz EM wave has little transmission loss in a dust environment and is beneficial for imaging in complex environments such as fire scenes, desert, and the battlefield. A photon has energy of 4.1 meV in the frequency of 1.0 THz, which is only about 1 ppm of that X-ray photon energy [7] and lower than the bond energy of various chemical bonds. Therefore, the THz EM wave does not cause photoionization and is very suitable for biopsies of human beings or other biological samples. Moreover, the THz EM wave would not penetrate the human skin and would be very safe for humans, owing to the strong absorption of the THz wave in the water [8,9]. It is an ideal tool for detecting skin cancers and cavities. The THz EM wave can be used as a communication carrier to carry more information per unit of time [10]. It is highly directional, which can be used for short-range directional secure communications in the battlefield.

A metamaterial is an artificially designed EM material with a periodic array structure, which can make THz EM waves couple with each other to generate particular optical characteristics [11–13], and then they possess extraordinary optical properties, such as negative magnetic permeability [14], negative conductivity [15], perfect lens [16], and so on. The metamaterial-based devices possess the merits of simple structure, small size, and high sensitivity. In order to enhance the performance of metamaterials, there are many literatures reported using various kinds of geometrical shapes, such as classical split-ring resonator (SRR), electric SRR, complementary SRR, three-dimensional (3D) SRR, etc. [17–27]. However, these metamaterial designs are limited to some simple applications and do not perform with multifunctional characteristics. Recently, metamaterials have been presented with dynamical tunability by using different materials [28–32], which can provide many applications, including optical switch, nanostructure sensors, and filters. However, these methods are lacking of optical-logic applications.

In this study, we present a flexible design by using a wrench-shape metamaterial (WSM) in the THz frequency range. It exhibits ultra-narrowband, polarization-dependent, switchable, and programmable characterizations. The resonant tuning ranges are 3.44 and 1.98 THz by changing geometrical

dimensions of WSM at the transverse electric (TE) and transverse magnetic (TM) modes, respectively. In these tuning ranges, the highest Q-factor of resonance is 47.73 at the TE mode. These multifunctional characteristics of the WSM device can be determined to represent the binary digits and then perform logic operations. Such a WSM device could potentially possess applicability, high portability, and cost-effectiveness to lay the foundation for the realization of programmable metamaterials.

Figure 1 shows the schematic drawing of the proposed WSM, which is composed of a tailored Au layer with 300 nm in thickness on a Si substrate. The permittivities of the Au layer and Si substrate are kept constant by increasing the monitored frequency. They are $10^4$ and 10 for the Au layer and Si substrate, respectively [33]. The denotations are arc radius ($r$), connector of arcs ($L$), arc angle ($\theta_1$), angle of incident light ($\theta_2$), and line width ($d$), respectively. Here, the line width of the WSM ($d$) is kept constant at 2.5 μm. The EM characteristics of WSM are performed by using Lumerical Solution's finite difference time-domain (FDTD) -based simulations to study the optical properties of devices. The propagation direction of the incident THz wave is perpendicular to the $x$–$y$ plane in the numerical simulations. Periodic boundary conditions are also adopted in the $x$ and $y$ directions, and perfectly matched layer (PML) boundaries conditions are assumed in the $z$ direction. The mesh precision is 0.5 nm with the minimum clearance size of 0.1 μm. It considers that the simulated results of the absorption spectra are nearly zero, and the results of the reflection spectra are supplementary to the transmission spectra. Therefore, we choose the transmission spectra to describe the optical characteristics of the WSM. The transmission THz wave is calculated by setting a monitor on the bottom side of the device. The transmission of the WSM can be represented by transmission matrix $T$ (solved by the Jones vector), which is described by Eqs. (1)–(3) [34]:

$$\begin{bmatrix} E_x^t \\ E_y^t \end{bmatrix} = T \begin{bmatrix} E_x^i \\ E_y^i \end{bmatrix} = \begin{bmatrix} t_{xx} & t_{xy} \\ t_{yx} & t_{yy} \end{bmatrix} \begin{bmatrix} E_x^i \\ E_y^i \end{bmatrix}, \tag{1}$$

$$t_{xx} = \frac{2Z_{xx}}{Z_{xx} + Z_0} D, \tag{2}$$

$$t_{yy} = \frac{2Z_{yy}}{Z_{yy} + Z_0} D, \tag{3}$$

where $E^i$ and $E^t$ are the components of the incident THz wave and the transmitted electric field, respectively. $E_x^i$, $E_y^i$, $E_x^t$ and $E_y^t$ are the corresponding $x$- and $y$-polarized components, respectively. $Z_{xx}$, $Z_{yy}$, and $Z_0$ are effective impedances for the $x$-polarization direction, $y$-polarization direction, and free space, respectively. $D$ is transmission loss including the absorptive loss and the reflection loss within the substrate.

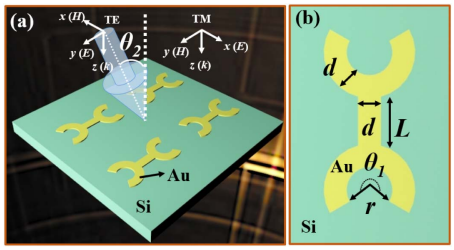


**Fig. 1.** (a) Schematic drawing of the WSM. (b) The denotations of geometrical parameters of the WSM unit cell.

Figure 2 shows the transmission spectra of the WSM by changing the $l$ value from 0 to 5.0 μm at the TE and TM modes. The other geometrical dimensions are kept as $r = 2.5$ μm, $\theta_1 = 240°$, and $\theta_2 = 0$ μm, respectively. In Fig. 2(a), the resonance is red-shifted 1.61 THz from 4.82 to 3.21 THz at the TE mode, and the corresponding $Q$-factors and transmittances of resonances are substantially kept as constant as 7.15 and 100%, respectively. At the TM mode, the resonance is blue-shifted 0.29 THz from 5.09 to 5.30 THz, and the corresponding $Q$-factors are kept constant at 11.54, as shown in Fig. 2(b). Figure 2(c) shows the zoom-in image of black dash—square region in Fig. 2(b). The corresponding $E$-field and $H$-field distributions are shown in Figs. 2(d) and 2(e) for the TE and TM modes, respectively. At the TE mode, the E-field energy is mainly distributed on the four apexes of the WSM, which has an electric quadrupole mode within the WSM unit cell, while the H-field energy is mainly concentrated on the center of the WSM device. At the TM mode, the $E$-field energy and $H$-field energy are distributed on the two sides of the WSM device, which has two dipoles within the WSM unit cell. According to the $E$- and $H$-field distributions of WSM, they can be explained as the corresponding resonances generated from the electric quadrupole mode and the dipole mode for TE and TM modes, respectively. It can be observed that the electrical quadrupole mode can be modified, and the dipole mode is kept stable by changing the $l$ value. Therefore, the EM responses at the TE mode exhibit more sensitivity than that at the TM mode.

Figure 3 shows the transmission spectra at the TE and TM modes by changing the $r$ value of the WSM from 0 to 5.0 μm. The other geometrical dimensions are kept at $l = 3$ μm, $\theta_1 = 240°$, and $\theta_2 = 0$, respectively. In Fig. 3(a), the resonance is red-shifted 0.17 THz from 3.81 to 3.64 THz by increasing the $r$ value from 1.0 to 3.5 μm at the TE mode. The zoom-in image of the black dash–square region of Fig. 3(a) is shown in Fig. 3(b). The corresponding $Q$-factors are substantially kept constant as 7.15. When $r = 4.0$ μm, the resonance is blue-shifted to 3.73 THz. At the TM mode, the resonance is red-shifted 4.40 THz from 8.30 to 3.90 THz by increasing the $r$ value from 1.0 to 4.0 μm, as shown in Fig. 3(c).

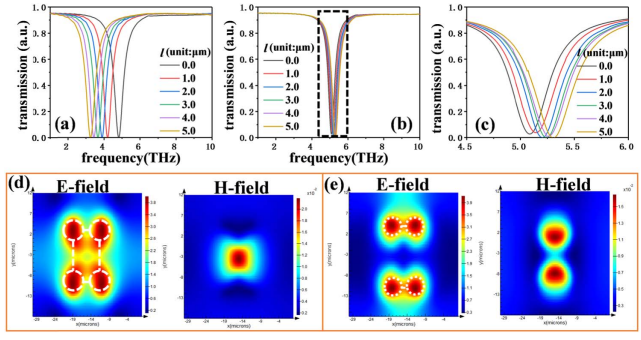


**Fig. 2.** Transmission spectra of the WSM at the (a) TE mode and (b) TM mode with different values. (c) Zoom-in image of black dash–square region of (b). (d) and (e) $E$-field and $H$-field distributions of (a) and (c), respectively.

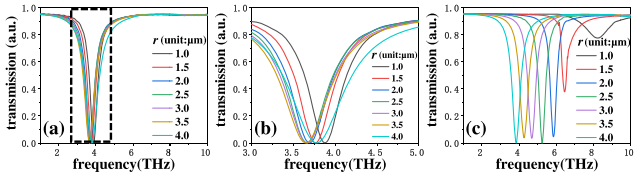


**Fig. 3.** Transmission spectra of the WSM with different $r$ values at (a) the TE mode. (b) The zoom-in image of black dash–square region of (a). (c) Transmission spectra of the WSM with different $r$ values at the TM mode.

The highest $Q$-factor is 6.77. The transmittances are almost kept as 95% in the range of $r = 2.0$–$4.0$ μm. According to the results of Figs. 2(d) and 2(e), the strongest $E$-field energies are focused on both ends of the WSM. It can be observed that the electric quadrupole mode can be modified clearly, and the dipole mode is modified less by changing the $r$ value. Therefore, the EM responses of the WSM with different $r$ values at the TM mode [Fig. 3(c)] exhibit more sensitivity than those at the TE mode [Fig. 3(a)].

Figure 4 shows the transmission spectra of the WSM with different $\theta_1$ values from 60° to 360° at the TE and TM modes. The other geometrical dimensions are kept at $l = 3.0$ μm, $r = 2.5$ μm, and $\theta_2 = 0°$, respectively. In Fig. 4(a), the resonance is red-shifted from 6.50 to 3.06 THz, and the bandwidth becomes broader at the TE mode. The corresponding $Q$-factors are in the range of 3.46–17.71. At the TM mode, when $\theta_1 = 60°$, 120°, and 360°, the EM responses are not evident while the resonance is red-shifted by increasing the $\theta_1$ value from 180° to 300°, as shown in Fig. 4(b). The corresponding $Q$-factor is in the range of 17.47–14.03.

Figure 5 shows the transmission spectra of the WSM with different $\theta_2$ values from 0° to 70° at the TE and TM modes. The other geometrical dimensions are kept at $l = 3.0$ μm, $r = 2.5$ μm, and $\theta_1 = 240°$, respectively. The resonances are very stable at 3.60 and 5.23 THz at the TE and TM modes, respectively. By increasing the $\theta_2$ value, the bandwidth of resonance becomes broader, and the transmission spectrum decreases gradually. The reason for such EM behavior is that even though the angle of incident light is altered, the polarization direction is kept parallel or vertical to the direction of arcs and gaps. This ensures that the structure remains a dipole and there is stable resonance, while the effective absorption area is larger, leading to the decline of the transmission with other no-resonance frequency spectra. The EM response of the WSM is omnidirectional and does not depend on the incident angle of the THz wave. Therefore, the WSM can be used for the THz opto-electronics with omnidirectional applications.

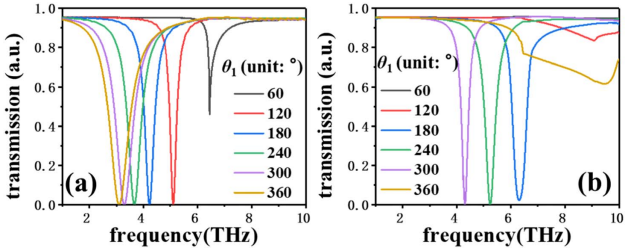


**Fig. 4.** Transmission spectra of the WSM at the (a) TE mode and (b) TM mode with different $\theta_1$ values.

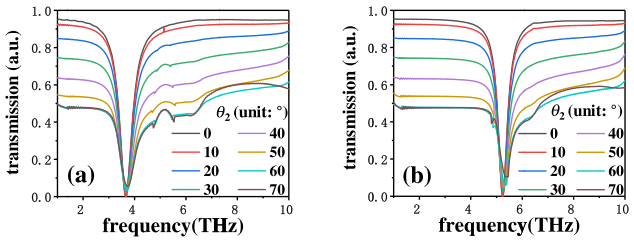


**Fig. 5.** Transmission spectra of the WSM at the (a) TE mode and (b) TM mode with different $\theta_2$ values, respectively.

Figure 6 shows the transmission spectra of the WSM with different configurations at the TE and TM modes. By configuring the unit cell from a single atom to a quad atom, the resonance is blue-shifted by 0.39 THz from 3.21 to 3.60 THz, and the resonant intensity becomes stronger at the TE mode. At the TM mode, the WSM with single-atom and interlaced arrangements show that there is not any EM response. Most of the incident THz wave is transmitted through the WSM. The other configurations exhibit a stable response at 5.23 THz. It shows obviously polarization-dependent characteristics. It means that the WSM possesses optical "on" and "off" states by configuring the WSM atoms with different arrangements. This superposition of resonances by different configurations provides the possibility of the WSM to be used as a programmable metamaterial to exhibit the binary digital signal "0" and "1", where the EM response of the WSM with a resonance corresponds to binary "1" and that without a resonance corresponds to binary "0". Figure 7 presents the characteristics of a programmable metamaterial using the WSM with different configurations, including one meta-atom along the $y$-axis direction and three meta-atoms along the $x$-axis direction. The geometrical dimensions are kept at $l = 3.0$ μm, $r = 2.5$ μm, $\theta_1 = 240°$, and $\theta_2 = 0°$, respectively. Each meta-atom can be controlled with a height ($h$) between the meta-atom and substrate. In Fig. 7(a), four meta-atoms are separated with an $h$ value of 1.0 μm, and the EM response shows no resonance. It can be denoted as the digital signal as "(0,0)". When the meta-atom along the $y$-axis direction is on the Si substrate, there is a resonance at 3.21 THz, as shown in Fig. 7(b).

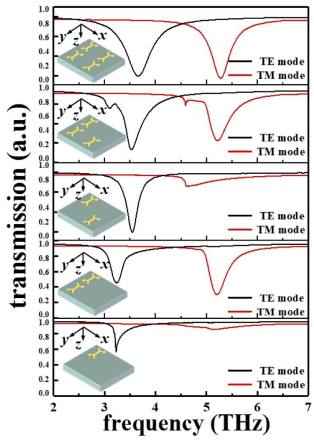


**Fig. 6.** Transmission spectra of the WSM with different configurations at the TE mode and TM mode.

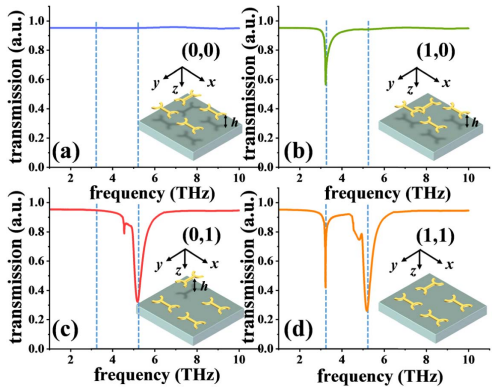


**Fig. 7.** Programmable metamaterial using the WSM configuration for (a) (0,0), (b) (1,0), (c) (0,1), and (d) (1,1), respectively.

It can be denoted as the digital signal as "(1,0)". Figure 7(c) shows that there are three meta-atoms along the $x$-axis direction on the Si substrate with a resonance at 5.23 THz. It can be denoted as the digital signal as "(0,1)". By designing four meta-atoms on the Si substrate, there are two resonances at 3.21 and 5.23 THz, which can be denoted as the digital signal as "(1,1)," as shown in Fig. 7(d). Such optical-logic behaviors exhibit the proposed WSM possessing multifunctionalities and provide the possibilities to be used for active sensors, optics digital processing, and modulators in the THz frequency range. As mentioned in the reported articles [35–37], programmable metamaterials have good regulatory characteristics and anti-interference, which can provide an important path to achieve full photoactivation.

In summary, we present a WSM device with actively high-efficiency tunability, large tuning range, and free composability. The WSM device exhibits the switch function of single-band to dual-band resonance with an ultra-narrow bandwidth. Q-factors of the WSM device with different deformations of $l$, $r$, $\theta_1$, and $\theta_2$ values are kept in the range of 3.5–48 and 4.8–18 at the TE mode and TM mode, respectively. Furthermore, the WSM device is omnidirectional, which is insensitive to the angle of the incident THz wave. By configuring the meta-atom arrangement, the WSM exhibits a programmable characteristic. It can be designed and tailored to be different digital signals. The design of the WSM opens an avenue to a new direction for future designs of optical applications to achieve more programmable optical devices. This work provides future tunable THz designs based on random combination mechanisms to deform the geometrical dimensions between WSM microstructures. Furthermore, it could potentially provide all-optical logical devices with precise tailoring of mechanical–optical properties and multichannel data processing at higher bit rates.

## REFERENCES


1. Y. S. Lin, F. Ma, and C. Lee, Opt. Lett. **38**, 3126 (2013).
2. J. L. Huang, J. S. Liu, K. J. Wang, Z. G. Yang, and X. M. Liu, Spectrochim. Acta A **198**, 198 (2018).
3. M. F. Kimmitt, J. Biol. Phys. **29**, 77 (2003).
4. M. Lee, H. E. Katz, C. Erben, D. M. Gill, P. Gopalan, J. D. Heber, and D. J. McGee, Science **298**, 1401 (2002).
5. P. Sookchoo, F. F. Sudradjat, A. M. Kiefer, H. Durmaz, R. Paiella, and M. G. Lagally, ACS Nano **7**, 2326 (2013).
6. D. R. Smith, J. B. Pendry, and M. C. K. Wiltshire, Science **305**, 788 (2004).
7. R. Yao, Q. Li, Q.-G. Yin, and Q. Wang, J. Appl. Opt. **30**, 233 (2009).
8. J. Y. Suen and W. J. Padilla, Appl. Phys. Lett. **108**, 233701 (2016).
9. D. S. Jessop, S. J. Kindness, L. Xiao, P. Braeuninger-Weimer, H. Lin, Y. Ren, C. X. Ren, S. Hofmann, J. A. Zeitler, H. E. Beere, D. A. Ritchie, and R. Degl'Innocenti, Appl. Phys. Lett. **108**, 171101 (2016).
10. Y. X. Zhang, Y. C. Zhao, S. X. Liang, B. Zhang, L. Wang, T. C. Zhou, W. Kou, F. Lan, H. X. Zeng, J. G. Han, Z. H. Feng, Q. Chen, P. Mazumder, and Z. Q. Yang, Nanophotonics **8**, 153 (2019).
11. W. C. Harris, D. D. Stancil, and D. S. Ricketts, Appl. Phys. Lett. **114**, 143903 (2019).
12. V. M. Shalaev, Nat. Photonics **1**, 41 (2007).
13. M. Choi, S. H. Lee, Y. Kim, S. B. Kang, J. Shin, M. H. Kwak, K. Y. Kang, Y. H. Lee, N. Park, and B. Min, Nature **470**, 369 (2011).
14. H. Ali, Plasmonics **14**, 91 (2019).
15. Y. Z. Cheng, X. Zuo, M. L. Huang, T. N. Wang, and R. Z. Gong, J. Infrared Millim. Terahertz Waves **38**, 97 (2019).
16. N. I. Landy, S. Sajuyigbe, J. J. Mock, D. R. Smith, and W. J. Padilla, Phys. Rev. Lett. **100**, 4 (2008).
17. C. Tan, Y. Wang, Z. M. Yan, X. Y. Nie, Y. H. He, and W. R. Chen, IEEE Trans. Appl. Supercond. **29**, 1500404 (2019).
18. T. P. Dave and J. M. Rathod, Int. J. RF Microw. Comput **29**, 10 (2019).
19. Y. S. Lin, S. Q. Liao, X. Y. Liu, Y. L. Tong, Z. F. Xu, R. J. Xu, D. Y. Yao, and Y. B. Yu, Opt. Laser Technol. **112**, 215 (2019).
20. P. Pitchappa, C. P. Ho, L. Dhakar, and C. Lee, Optica **2**, 571 (2015).
21. P. Pitchappa, C. P. Ho, L. Cong, R. Singh, N. Singh, and C. Lee, Adv. Opt. Mater. **4**, 391 (2016).
22. P. Pitchappa, M. Manjappa, C. P. Ho, R. Singh, N. Singh, and C. Lee, Adv. Opt. Mater. **4**, 541 (2016).
23. P. Pitchappa, M. Manjappa, C. P. Ho, R. Singh, N. Singh, and C. Lee, Appl. Phys. Lett. **109**, 211103 (2016).
24. L. Cong, P. Pitchappa, C. Lee, and R. Singh, Adv. Mater. **29**, 1700733 (2017).
25. L. Cong, P. Pitchappa, Y. Wu, L. Ke, C. Lee, N. Singh, H. Yang, and R. Singh, Adv. Opt. Mater. **5**, 1600716 (2017).
26. M. Manjappa, P. Pitchappa, N. Wang, C. Lee, and R. Singh, Adv. Opt. Mater. **6**, 1800141 (2018).
27. M. Manjappa, P. Pitchappa, N. Singh, N. Wang, N. I. Zheludev, C. Lee, and R. Singh, Nat. Commun. **9**, 4056 (2018).
28. A. Farmani, IEEE Photonics Technol. Lett. **31**, 643 (2019).
29. A. Farmani, A. Mir, and Z. Sharifpour, Appl. Surf. Sci. **453**, 358 (2018).
30. A. Farmani, J. Opt. Soc. Am. B **36**, 401 (2019).
31. A. Farmani, M. Miri, and M. H. Sheikhi, IEEE Photonics Technol. Lett. **30**, 153 (2018).
32. A. Farmani, M. Miri, and M. H. Sheikhi, J. Opt. Soc. Am. B **34**, 1097 (2017).
33. https://www.fzu.cz/~dominecf/eps/index.html.
34. J. F. O'Hara, E. Smirnova, A. K. Azad, H.-T. Chen, and A. J. Taylor, Act. Passive Electron. Compon. **2007**, 49691 (2007).
35. K. L. Shih, P. Pitchappa, M. Manjappa, C. P. Ho, R. Singh, B. Yang, N. Singh, and C. Lee, Appl. Phys. Lett. **110**, 161108 (2017).
36. A. X. Lalas, N. V. Kantartzis, and T. D. Tsiboukis, COMPEL **35**, 1460 (2016).
37. A. Lalas, N. Kantartzis, and T. Tsiboukis, Appl. Phys. A **117**, 433 (2014).